Physics of Fluids

Study of instabilities and quasi-two-dimensional turbulence in volumetrically heated magnetohydrodynamic flows in a vertical rectangular duct

N. Vetcha, S. Smolentsev, M. Abdou, and R. Moreau

Citation: Phys. Fluids 25, 024102 (2013); doi: 10.1063/1.4791605
View online: http://dx.doi.org/10.1063/1.4791605
View Table of Contents: http://pof.aip.org/resource/1/PHFLE6/v25/i2
Published by the American Institute of Physics.

PHYSICS OF FLUIDS **25**, 024102 (2013)

Study of instabilities and quasi-two-dimensional turbulence in volumetrically heated magnetohydrodynamic flows in a vertical rectangular duct

N. Vetcha,[1] S. Smolentsev,[1,a)] M. Abdou,[1] and R. Moreau[2]
[1]*Mechanical and Aerospace Engineering Department, University of California, Los Angeles, California 90095, USA*
[2]*Laboratoire EPM, ENSHMG, BP 95, 38402 Saint-Martin d'Hères, France*

(Received 31 July 2012; accepted 17 January 2013; published online 15 February 2013)

We consider magnetohydrodynamic (MHD) rectangular duct flows with volumetric heating. The flows are upward, subject to a strong transverse magnetic field perpendicular to the temperature gradient, such that the flow dynamics is quasi-two-dimensional. The internal volumetric heating imitates conditions of a blanket of a fusion power reactor, where a buoyancy-driven flow is imposed on the forced flow. Studies of this mixed-convection flow include analysis for the basic flow, linear stability analysis and Direct Numerical Simulation (DNS)-type computations. The parameter range covers the Hartmann number (Ha) up to 500, the Reynolds number (Re) from 1000 to 10 000, and the Grashof number (Gr) from 10^5 to 5×10^8. The linear stability analysis predicts two primary instability modes: (i) bulk instability associated with the inflection point in the velocity profile near the "hot" wall and (ii) side-wall boundary layer instability. A mixed instability mode is also possible. An equation for the critical Hartmann number has been obtained as a function of Re and Gr. Effects of Ha, Re, and Gr on turbulent flows are addressed via nonlinear computations that demonstrate two characteristic turbulence regimes. In the "weak" turbulence regime, the induced vortices are localized near the inflection point of the basic velocity profile, while the boundary layer at the wall parallel to the magnetic field is slightly disturbed. In the "strong" turbulence regime, the bulk vortices interact with the boundary layer causing its destabilization and formation of secondary vortices that may travel across the flow, even reaching the opposite wall. In this regime, the key phenomena are vortex-wall and various vortex-vortex interactions. Flow and magnetic field effects on heat transfer are also analyzed. [http://dx.doi.org/10.1063/1.4791605]

I. INTRODUCTION

In this study we focus on instability and turbulence phenomena in rectangular duct flows of viscous, incompressible, electrically conducting fluid with volumetric heating subject to a strong uniform transverse magnetic field, such that a quasi-two-dimensional (Q2D) flow regime (see, e.g., Ref. 1) is enforced. Such Q2D instabilities and transition to turbulence are likely to occur in conditions of a liquid metal blanket, in particular, in poloidal ducts of the so-called dual-coolant lead-lithium (DCLL) blanket (see, e.g., Ref. 2), where eutectic alloy lead-lithium circulates as breeder/coolant in the presence of a strong plasma-confining magnetic field. The reference flow is sketched in Fig. 1, which also shows the volumetric heating profile, the coordinate axes and the direction of the applied magnetic field $\mathbf{B_0}$. Present considerations are limited to vertical upward flows (buoyancy-assisted flows) in a duct with ideally insulating walls, both thermally and electrically. The distribution of the

a)Author to whom correspondence should be addressed. Electronic mail: sergey@fusion.ucla.edu.

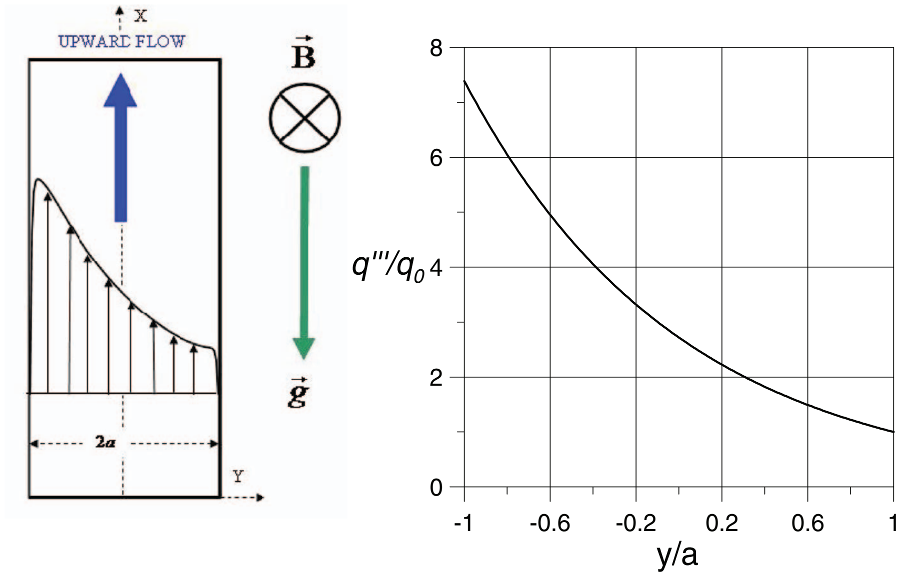

FIG. 1. Sketch illustrating the forced flow direction with respect to the gravity vector and magnetic field (left) and volumetric heating profile (right).

volumetric heat imitates the exponentially decaying heating profile typical to blanket conditions, due to the slowing down of plasma neutrons, in the form

$$q'''(y) = q_0 \exp\left(-\frac{y+a}{l}\right), \tag{1}$$

where a is half of the duct width in the direction perpendicular to the applied field, l is the decay length, and q_0 is the maximum volumetric heating at the "hot" wall $y = -a$. This distribution of the volumetric heat is responsible for buoyancy forces in the liquid, which result in asymmetric velocity profiles with a higher velocity at the hot wall and lower velocity at the "cold" wall $y = a$ as shown in Fig. 1. The reference flow is the superposition of a forced flow with the mean bulk velocity U_m and a buoyancy-driven flow, a regime known as a mixed-convection flow. In this regime, the velocity profile has one or more inflection points and thus the flow is subject to Kelvin-Helmholtz (inflectional) instability and eventually can transition to turbulence, which in the reference conditions takes a special Q2D form as described in Ref. 1.

Instabilities and transitions in MHD flows with a symmetric "M-shaped" velocity profile have recently been studied in Ref. 3 for a family of Q2D flows, where the basic velocity profiles with near-wall jets and associated points of inflection were produced by imposing an external flow-opposing force. By varying this force and position of the inflection point, various instability modes and transition scenarios were modeled. Among the most interesting observations in Ref. 3 is the interaction of the bulk vortices associated with the inflection point with the boundary layer at the duct wall parallel to the applied magnetic field (side or Shercliff layer) that causes a secondary instability and eventually a transition to Q2D turbulence. Similar instabilities can be envisaged in the reference mixed-convention flow but details can be different, first of all due to strong asymmetry in the basic velocity profile and also due to the effect of the flow velocity, heating, and the magnetic field strength on the position of the inflection point with respect to the duct walls. Several studies of buoyancy-driven MHD flows in vertical ducts have been performed in the recent past (see, e.g., Refs. 4–6), but MHD mixed convection in the presence of a transverse magnetic field, in particular unsteady phenomena, has not been systematically addressed, except for some initial considerations by the authors themselves (see Refs. 2, 7, and 8). In this paper in order to address this kind of phenomena, we use analytical and numerical approaches similar to those in Ref. 3, including the full analytical solution for the basic velocity profile, a linear stability analysis, and a nonlinear

DNS-type computations. The model and basic assumptions are introduced in Sec. II. An analytical solution for the unperturbed basic flow is given in Sec. III. Section IV includes the linear stability analysis of the perturbed flow based on the numerical solution of the associated Orr-Sommerfield (OS) problem. Nonlinear DNS-type computations are performed in Sec. V. Finally, the obtained results are summarized in Sec. VI.

II. PROBLEM FORMULATION

Present analysis of instabilities and transitions in the reference MHD mixed-convection flow sketched in Fig. 1 is based on the idea of a Q2D MHD flow, which in the most complete form is formulated in Ref. 1. In accordance with this concept, a strong magnetic field enforces the liquid motion to occur mostly in the planes perpendicular to the applied magnetic field, while the flow along the magnetic field lines is damped. The important 3D effects are still localized within the thin Hartmann layers at the duct walls perpendicular to the applied magnetic field, where most of the dissipation losses occur. The Q2D turbulent structures appear as columnar-like vortices aligned with the field direction and are subject to an inverse energy cascade. Their intensity is a result of the balance between the Joule and viscous dissipation in the Hartmann layers, on the one hand, and the energy feeding mechanism associated with the instability, on the other hand. Such Q2D eddies can be highly energetic, occupy the whole cross-section of the duct and persist over many eddy turnovers. In experiments, these striking Q2D properties were first studied in Ref. 9 and later in many other laboratory experiments and 3D numerical simulations.

A model for Q2D non-isothermal MHD flows for the case when the applied magnetic field is perpendicular to the temperature gradient has been formulated in Refs. 5 and 6 for natural-convection flows and is also adopted here for mixed-convection flows. In the particular case of isothermal Q2D MHD flows, the velocity profile in the magnetic field direction is known to be of the Hartmann type, i.e., there are two thin Hartmann boundary layers at the walls perpendicular to the applied magnetic field where the velocity grows exponentially from zero at the wall to the core value, and the core region itself where the velocity is uniform. In this case, averaging the full 3D momentum equation gives rise to the additional friction term linear in the velocity (see Ref. 1). Compared to purely isothermal MHD flows, in the reference case of buoyancy-driven flows, the original 3D momentum equation includes an extra term, which arises from the buoyancy force. Moreover, the Hartmann layers themselves can be modified if the buoyancy forces are present and strong. The uniformity of the temperature profile in the magnetic field direction may also be questioned since near the Hartmann walls the balance between volumetric heating and streamwise convective heat flux is not hold compared to that in the flow in the core region, because the velocity in the boundary layer is lower. The detailed order of magnitude analysis performed in Refs. 5 and 6 shows, however, that the Hartmann layers are just slightly modified by the buoyancy forces such that an additional correction term is of the order of $1/Ha$ and thus can be neglected for all natural- or mixed-convection flows as long as $Ha \gg 1$. Temperature uniformity in the magnetic field direction has also been justified in Refs. 5 and 6. In fact, it has been demonstrated that the Q2D model for buoyancy-driven flows exhibits unsteadiness and turbulence in good agreement with the 3D numerical predictions and experimental data as soon as $Ha > 30$. In the present study, some 3D computations were also performed using the MHD solver HIMAG (Ref. 10), mostly to re-confirm that the basic Q2D model assumptions are also valid for the reference mixed-convection flows. In these computations, a MHD mixed-convection flow in a long vertical insulating duct with two radial sections is considered (Fig. 4(a)). The computed results do confirm that the velocity distribution does not experience significant variations in the direction of the applied magnetic field except for the thin Hartmann layers. The temperature distribution is also rather uniform in the field direction, even in the Hartmann layers. The flow also demonstrates near fully developed behavior over the significant part of the vertical section.

Providing the applied magnetic field is strong enough, the reference mixed-convection flow is governed by the following four Q2D equations (2)–(5) written in terms of the bulk velocity components $U(x, y)$ and $V(x, y)$, pressure $P(x, y)$, and the temperature $T(x, y)$ using the Boussinesq approximation for the buoyant force:

$$\frac{\partial U}{\partial t} + U\frac{\partial U}{\partial x} + V\frac{\partial U}{\partial y} = -\frac{1}{\rho}\frac{\partial P}{\partial x} + \nu\left(\frac{\partial^2 U}{\partial x^2} + \frac{\partial^2 U}{\partial y^2}\right) - \frac{U}{\tau} - g + g\beta(T - \bar{T}), \tag{2}$$

$$\frac{\partial V}{\partial t} + U\frac{\partial V}{\partial x} + V\frac{\partial V}{\partial y} = -\frac{1}{\rho}\frac{\partial P}{\partial y} + \nu\left(\frac{\partial^2 V}{\partial x^2} + \frac{\partial^2 V}{\partial y^2}\right) - \frac{V}{\tau}, \tag{3}$$

$$\frac{\partial U}{\partial x} + \frac{\partial V}{\partial y} = 0, \tag{4}$$

$$\rho C_p\left(\frac{\partial T}{\partial t} + U\frac{\partial T}{\partial x} + V\frac{\partial T}{\partial y}\right) = k\left(\frac{\partial^2 T}{\partial x^2} + \frac{\partial^2 T}{\partial y^2}\right) + q'''. \tag{5}$$

Here, ρ, ν, σ, k, C_p, and β are the fluid density, kinematic viscosity, electrical conductivity, thermal conductivity, specific heat, and the volumetric thermal expansion coefficient correspondingly, g is the gravitational acceleration, $\bar{T}(x) = \frac{1}{2a}\int_{-a}^{a} T(x, y)dy$ is the mean temperature in the liquid, and $\tau = bB_0^{-1}\sqrt{\frac{\rho}{\sigma\nu}}$ is the so-called "Hartmann braking time" (see Ref. 1), which is a time-scale for vortex damping due to ohmic and viscous losses in the Hartmann layers. The dimension b is half of the duct width in the direction of the applied magnetic field. The five dimensionless parameters that characterize the problem are: the Hartmann number $Ha = B_0 b\sqrt{\frac{\sigma}{\nu\rho}}$ (Hartmann number squared is the ratio of the electromagnetic to viscous force), the hydrodynamic Reynolds number $Re = \frac{U_m a}{\nu}$ (the ratio of the inertia to viscous force), the Grashof number $Gr = \frac{g\beta\Delta T a^3}{\nu^2}$ (represents the ratio of the buoyancy to viscous force), the duct aspect ratio a/b, and the Prandtl number $Pr = \nu\rho C_p/k$. Three more dependent parameters are also used: the interaction parameter (Stuart number) $N = Ha^2/Re$, the Peclet number $Pe = RePr$, and the Rayleigh number $Ra = GrPr$. The temperature scale is defined here through the average volumetric heating $\bar{q} = (2a)^{-1}\int_{-a}^{a} q'''(y)dy$ as $\Delta T = \bar{q}a^2/k$. The applicability of this model to unsteady vortical MHD flows generally depends on the difference between the time needed to establish two-dimensionality and the characteristic eddy turnover time. Generally, transition from 3D to Q2D flow occurs if the magnetic field is strong enough. For forced convection MHD flows, this requires $N \gg 1$ (Ref. 1), and for natural-convection MHD flows the requirement is $Ha^2 > 4\sqrt{Gr}$ as suggested in Ref. 6. One more limitation is related to the Hartmann layer, which is required to be laminar to assure a simple exponential velocity distribution near the wall adopted in the model. In accordance with the experimental data in Ref. 11, the Hartmann boundary layer remains laminar providing $Ha/Re > 150$–250. In all nonlinear DNS-type computations shown below in Sec. V, the goal was to keep all the parameters in the range where the Q2D model is valid. The dominance of Q2D flow dynamics in the reference flow was also directly confirmed for several combinations of Ha, Re, and Gr numbers via comparisons with the full 3D numerical solutions in Ref. 12.

III. BASIC FLOW SOLUTION

In a fully established mixed-convection flow, the velocity component V is zero and both the pressure and the velocity component U are independent of the cross-axial coordinate y, so that the mathematical model can further be simplified by decomposing the temperature field into the mean $\bar{T}(x)$ and cross-axial $\theta(y)$ components:

$$T(x, y) = \bar{T}(x) + \theta(y). \tag{6}$$

In turn, the mean temperature can be deduced from the global energy balance in the flow as $\bar{T}(x) = T_0 + \frac{\bar{q}}{\rho C_p U_m}x$, where T_0 is the temperature at the flow inlet at $x = 0$. In addition, the pressure term can be written as

$$P(x) = P_0 - \rho(G + g)x, \tag{7}$$

where P_0 is the inlet pressure and G is a constant, which needs to be determined. After substitution of Eqs. (6) and (7) into Eqs. (2) and (5), the two equations can be combined into one forth-order ordinary differential equation as follows:

$$\theta^{IV} - Ha\left(\frac{a}{b}\right)^2\theta'' + \frac{Gr}{Re}\theta = -G_* + \frac{2m}{1-e^{-2m}}e^{-m(y+1)}\left[Ha\left(\frac{a}{b}\right)^2 - m^2\right]. \tag{8}$$

Equation (8) is written in a dimensionless form, using ΔT as a temperature scale and the duct dimension a as a length scale. Here, $G_* = Ga^2/(\nu U_m)$ and $m = a/l$ are also dimensionless. Once the temperature $\theta(y)$ is known, the velocity can be found using the following formula:

$$U = \theta'' + \frac{2m}{1-e^{-2m}}e^{-m(y+1)}, \tag{9}$$

where U_m is used as a velocity scale. The boundary conditions come from the no-slip and ideal thermal insulation conditions:

$$\theta'\big|_{y=\pm1} = 0, \quad \theta''\big|_{y=-1} = -\frac{2m}{1-e^{-2m}}, \quad \theta''\big|_{y=+1} = -\frac{2m}{1-e^{-2m}}e^{-2m}. \tag{10}$$

A. Full solution

In accordance with the common theory, a general solution for Eq. (8) is of the form

$$\theta(y) = -\frac{Re}{Gr}G_* + \frac{2m/(1-e^{-2m})[Ha(a/b)^2 - m^2]}{m^4 - Ha(a/b)^2m^2 + Gr/Re}e^{-m(y+1)} + \sum_{i=1}^{4}A_i f_i(y+1). \tag{11}$$

In this solution, the first two terms represent a particular solution, while f_i ($i = 1$–4) are linearly independent solutions of the uniform equation obtained from Eq. (8). The four coefficients A_i need to be found from boundary conditions (10). In turn, the four solutions f_i depend on the roots of the biquadratic characteristic equation:

$$\lambda^4 - Ha\left(\frac{a}{b}\right)^2\lambda^2 + \frac{Gr}{Re} = 0. \tag{12}$$

The roots themselves depend on the sign of the discriminant $D = Ha^2\,(a/b)^4 - 4\frac{Gr}{Re}$, which is built of two characteristic length scales: $1/\sqrt{Ha}$ stands for the dimensionless thickness of the side layer in a purely MHD flow, and $(Re/Gr)^{1/4}$ characterizes the thickness of the boundary layer in a mixed-convection flow without a magnetic field. In the case $D > 0$, all roots are real:

$$\lambda_{1,2} = \pm[\frac{1}{2}(Ha(\frac{a}{b})^2 + \sqrt{Ha^2(\frac{a}{b})^4 - 4\frac{Gr}{Re}})]^{1/2}, \lambda_{3,4} = \pm[\frac{1}{2}(Ha(\frac{a}{b})^2 - \sqrt{Ha^2(\frac{a}{b})^4 - 4\frac{Gr}{Re}})]^{1/2},$$

so that $f_1 = e^{\lambda_1(y+1)}$, $f_2 = e^{\lambda_2(y+1)}$, $f_3 = e^{\lambda_3(y+1)}$, $f_4 = e^{\lambda_4(y+1)}$. In the case $D = 0$, there are two double real roots $\lambda_{1,2} = \pm\frac{\sqrt{2}}{2}\sqrt{Ha}\frac{a}{b}$ and the four solutions are: $f_1 = e^{\lambda_1(y+1)}$, $f_2 = e^{\lambda_2(y+1)}$, $f_3 = (y+1)e^{\lambda_1(y+1)}$, $f_4 = (y+1)e^{\lambda_2(y+1)}$. In the case $D < 0$, there are four complex roots $\lambda_{1,2} = \alpha \pm i\beta$, $\lambda_{3,4} = -\alpha \pm i\beta$, where $\alpha = \sqrt{\frac{1}{4}Ha(a/b)^2 + \frac{1}{2}\sqrt{Gr/Re}}$, $\beta = \sqrt{\frac{4Gr/Re - Ha^2(a/b)^4}{8\sqrt{Gr/Re} + 4Ha(a/b)^2}}$, so that

$$f_1 = e^{\lambda_1(y+1)}\cos[\beta_1(y+1)],\ f_2 = e^{\lambda_1(y+1)}\sin[\beta_1(y+1)],$$
$$f_3 = e^{\lambda_2(y+1)}\cos[\beta_2(y+1)],\ f_4 = e^{\lambda_2(y+1)}\sin[\beta_2(y+1)].$$

The coefficients A_i have been evaluated using Wolfram's MATHEMATICA (Ref. 13) and the constant G_* (not shown here) is calculated using the condition $\int_{-a}^{a}\theta(y)dy = 0$.

B. Approximate solution

At high Hartmann numbers Eq. (8) can be simplified by neglecting the fourth-order derivative θ^{IV}. Based on the relation between U and θ [see Eq. (9)] neglecting this derivative is equivalent to neglecting the second derivative U'' in the momentum equation. The physical reason for dropping these terms is the small thickness of the side-wall boundary layer such that the flow rate carried by the boundary layer is insignificant compared to the bulk flow, and also due to the fact that the viscous friction here is negligible compared to that in the Hartmann layer. Solving the obtained simplified problem is straightforward:

$$\theta(y) = \frac{2m^2}{r(r^2-m^2)(1-e^{-2m})}\left(\frac{e^{-2m}\cosh[r(y+1)] - \cosh[r(y-1)]}{\sinh(2r)}\right) + \frac{2me^{-m(y+1)}}{(r^2-m^2)(1-e^{-2m})} - \frac{1}{r^2}, \tag{13}$$

$$U(y) = 1 + r^2\theta(y). \tag{14}$$

It is notable that the approximate solution includes only two dimensionless parameters: $r = \sqrt{\frac{Gr}{HaRe(a/b)^2}}$ and m. The shape parameter m affects the steepness of the heating profile. In the blanket conditions it is fully determined by the interaction of neutrons with the liquid metal. Parameter r is more related to the liquid metal flow itself as it carries information on the contribution of various forces acting on the flow. In the particular DCLL blanket design, $m \approx 1$ and $r = 5$–40 (Ref. 2). These values are used in all further computations. Also, $a/b = 1$ is assumed in all computations. In accordance with the obtained solution, higher velocity occurs at the hot wall, where volumetric heating reaches its maximum, often in the form of a high-velocity near-wall jet. As seen from the simplified solution, the difference between the maximum velocity at the hot wall $U_{\max}$ and the minimum one at the cold wall $U_{\min}$ increases with r approaching the asymptotic value when $r \gg 1$:

$$U_{\max} - U_{\min} = 2m. \tag{15}$$

C. Comparisons between full, approximate, and 3D numerical solutions

Typical velocity and temperature profiles calculated with the full and simplified solutions are shown in Fig. 2 for three special cases: $D \gg 0$, $D = 0$, and $D \ll 0$. If $D \gg 0$, the solution in the near-wall region is dominated by the exponential term $e^{\sqrt{Ha}(a/b)(1+y)}$, which represents the well-known distribution in the MHD Shercliff layer. In this case, distinctive Shercliff layers can be seen with the thickness scaled as $1/\sqrt{Ha}$. In the bulk, the velocity and the temperature both drop in a similar manner.

Based on the full solution, the velocity profiles in this case demonstrate two inflection points located in the flow bulk.

In the opposite case $D \ll 0$, the solution near the wall is described by the exponential term $e^{0.5\sqrt{2}(Gr/Re)^{1/4}(1+y)}$ such that the thickness of the boundary layer is scaled as $(Re/Gr)^{1/4}$. In this case, a distinctive high-velocity jet can be seen near the hot wall and a smaller jet near the cold wall. The number of inflection points in this case can vary from 2 to 6. The major inflection point, where the vorticity is maximum, is always located on the bulk-side leg of the larger jet. Examples of flows with two or more (up to six) inflection points in the velocity profile, also based on the full solution, are shown in Table I.

In this case, the temperature profile demonstrates an almost flat distribution in the bulk and two asymmetric peaks near the walls.

The case $D = 0$ demonstrates intermediate features between the cases $D \ll 0$ and $D \gg 0$. Taking into account that the nature of the boundary layer at the side wall is not necessarily fully controlled by MHD effects, in what follows we will refer to this layer as just a boundary layer or a side-wall boundary layer rather than side or Shercliff layer, which applies to purely isothermal MHD flows. In all three cases, there is a fair match between the simplified and the full solutions in the bulk. This allows for using the simplified solution for a kind of express analysis since it is much more compact compared to the lengthy full solution. The importance of the simplified solution is also in a reduction of four dimensionless parameters into one dimensionless group r as discussed above.

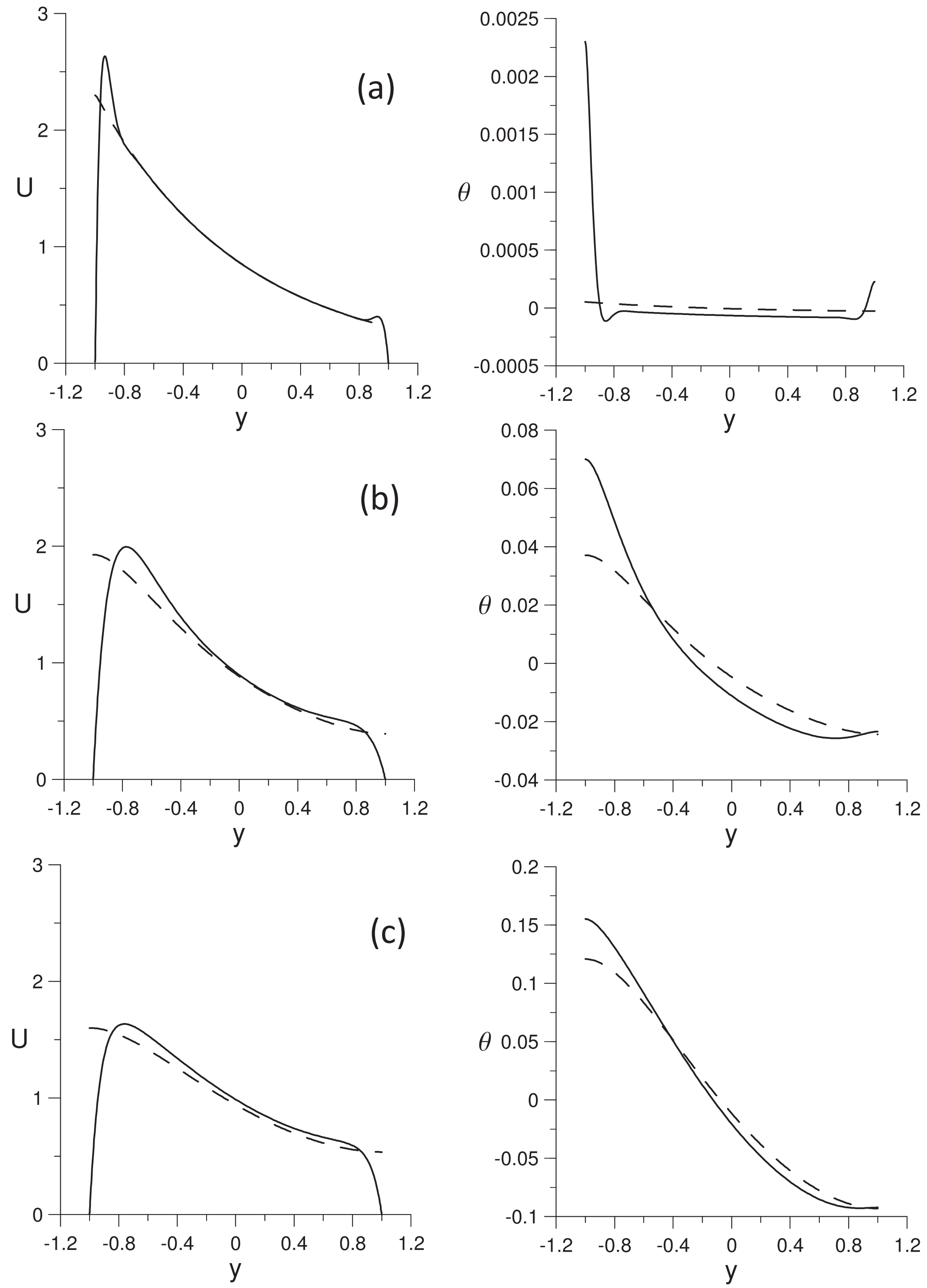

FIG. 2. Comparison of velocity and temperature profiles calculated with the full (solid line) and simplified (dashed line) solutions: (a) $D \ll 0$: $Ha = 40$, $Gr = 10^9$, $Re = 1000$, $r = 158.1$; (b) $D = 0$: $Ha = 100$, $Gr = 2.5 \times 10^7$, $Re = 10{,}000$, $r = 5$; and (c) $D \gg 0$: $Ha = 200$, $Gr = 10^7$, $Re = 10\,000$, $r = 2.23$.

TABLE I. Location of inflection points and associated vorticity in the basic velocity profile.

Ha	*Gr*	*Re*	Point 1	Point 2	Point 3	Point 4	Point 5	Point 6
50	10^8	5000	$y = -0.726$ $\omega = 3.927$	$y = 0.740$ $\omega = 0.089$	...	...	...	...
100	2.5×10^7	10 000	$y = -0.574$ $\omega = 1.948$	$y = 0.646$ $\omega = 0.291$	...	...	...	...
75	8×10^8	2000	$y = -0.866$ $\omega = 7.208$	$y = -0.666$ $\omega = 1.489$	$y = -0.606$ $\omega = 1.507$	$y = 0.866$ $\omega = -0.353$	...	...
100	3×10^9	5000	$y = -0.880$ $\omega = 7.760$	$y = -0.700$ $\omega = 1.529$	$y = -0.633$ $\omega = 1.563$	$y = 0.880$ $\omega = -0.429$	...	...
40	10^9	1000	$y = -0.896$ $\omega = 8.879$	$y = -0.746$ $\omega = 1.524$	$y = -0.666$ $\omega = 1.632$	$y = 0.694$ $\omega = 0.437$	$y = 0.738$ $\omega = 0.440$	$y = 0.896$ $\omega = -0.575$
75	2×10^9	2000	$y = -0.893$ $\omega = 8.717$	$y = -0.740$ $\omega = 1.543$	$y = -0.666$ $\omega = 1.631$	$y = 0.700$ $\omega = 0.437$	$y = 0.733$ $\omega = 0.439$	$y = 0.893$ $\omega = -0.556$

The location of the major inflection point d where the vorticity is maximum with respect to the wall and associated maximum vorticity $\omega_{\max}$ are of particular interest since these two parameters can affect flow stability and, as shown in Ref. 3, be responsible for the transition scenario. The associated data are extracted from the full solution and plotted in Fig. 3 to illustrate the effect of *Gr*, *Re*, and *Ha*. The increase in *Re* results in shifting the inflection point from the wall towards the axis and reduces the vorticity. The effect of the Hartmann number on vorticity is similar. The position of the inflection point itself is however only slightly affected by *Ha*. Increasing *Gr* results in a significant increase of vorticity while the inflection point moves from the axis to the wall.

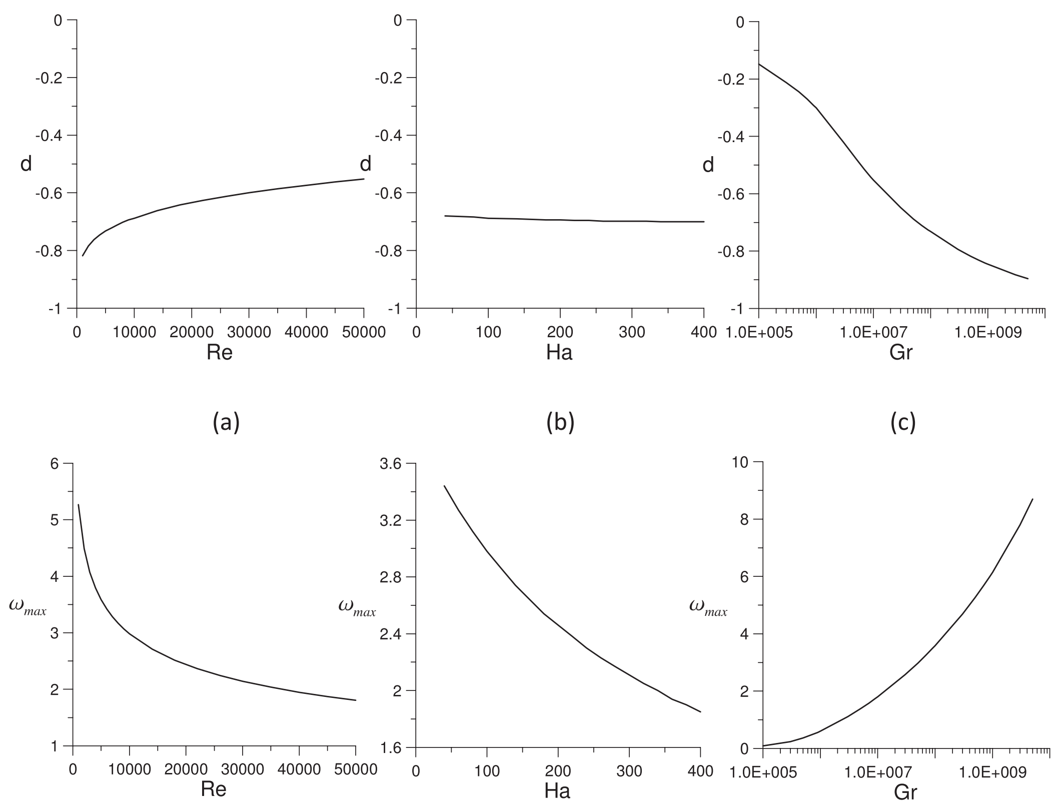

FIG. 3. Effect of the flow parameters on the location of the major inflection point (top row) and the vorticity (bottom row): (a) effect of *Re*: $Ha = 100$, $Gr = 10^8$; (b) effect of *Ha*: $Gr = 10^8$, $Re = 10\,000$; and (c) effect of *Gr*: $Ha = 100$, $Re = 5000$.

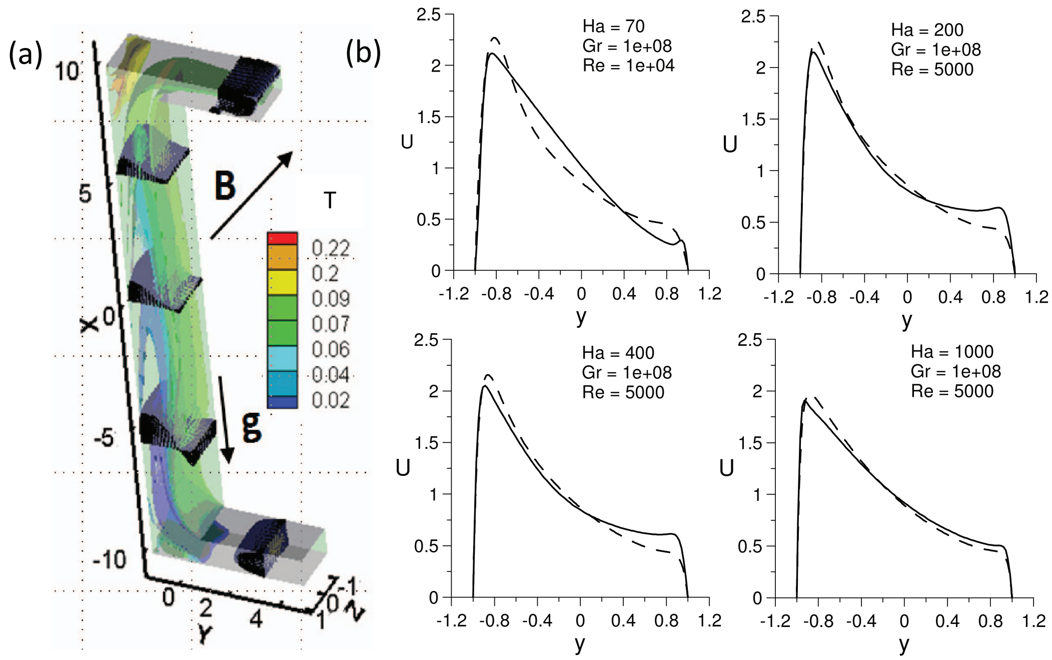

FIG. 4. MHD mixed-convection flow in a square vertical duct: (a) 3D velocity vectors and temperature counters for $Ha = 70$, $Re = 10^4$, and $Gr = 10^8$; (b) comparison between 3D at $x = 4$ (solid line) and full 1D analytical (dashed line) solutions.

In addition, comparisons for the basic velocity profile are made between the 1D full analytical solution and 3D numerical results (Fig. 4(b)) for several combinations of the flow parameters. Within the duct length where the 3D flow is fully developed, these comparisons demonstrate fair agreement.

IV. LINEAR STABILITY ANALYSIS

Equations (2), (3), and (5) are changed to the equivalent form using the vorticity ω ($\omega = \frac{\partial V}{\partial x} - \frac{\partial U}{\partial y}$), the streamfunction ψ ($U = \frac{\partial \psi}{\partial y}, V = -\frac{\partial \psi}{\partial x}$), and the cross-axial temperature θ ($\theta = T - \bar{T}$). Written in a dimensionless form, these equations are as follows:

$$\frac{\partial \omega}{\partial t} + \frac{\partial \psi}{\partial y}\frac{\partial \omega}{\partial x} - \frac{\partial \psi}{\partial x}\frac{\partial \omega}{\partial y} = \frac{1}{Re}\left(\frac{\partial^2 \omega}{\partial x^2} + \frac{\partial^2 \omega}{\partial y^2}\right) - \frac{Ha}{Re}\left(\frac{a}{b}\right)^2 \omega - \frac{Gr}{Re^2}\frac{\partial \theta}{\partial y}, \tag{16}$$

$$\frac{\partial^2 \psi}{\partial x^2} + \frac{\partial^2 \psi}{\partial y^2} = -\omega, \tag{17}$$

$$\frac{\partial \theta}{\partial t} + \frac{\partial \psi}{\partial y}\frac{\partial \theta}{\partial x} - \frac{\partial \psi}{\partial x}\frac{\partial \theta}{\partial y} = \frac{1}{RePr}\left(\frac{\partial^2 \omega}{\partial x^2} + \frac{\partial^2 \omega}{\partial y^2} - U\right) + \frac{1}{RePr}\frac{2m}{1 - e^{-2m}}e^{-m(y+1)}. \tag{18}$$

The time-dependent solution can be expanded in normal modes such that

$$[\psi(x, y, t), \omega(x, y, t), \theta(x, y, t)] = [\psi_0(y), \omega_0(y), \theta_0(y)] + [\psi_1(y), \omega_1(y), \theta_1(y)]e^{i(\alpha x - \beta t)}. \tag{19}$$

Here, $\psi_0(y)$, $\omega_0(y)$, $\theta_0(y)$ are the basic solutions, while $\psi_1(y)$, $\omega_1(y)$, $\theta_1(y)$ are the infinitesimal amplitudes of the perturbations. The wavelength of the disturbance λ is related to the wavenumber α, which is real, as $\lambda = 2\pi/\alpha$. The parameter β as well as the ratio $s = \beta/\alpha$ are complex: $\beta = \beta_r + i\beta_i$ and $s = s_r + is_i$. The real part s_r is the phase velocity of the disturbance in the axial direction. The imaginary part s_i determines whether the perturbation is amplified or damped with time, if $s_i > 0$ ($\beta_i > 0$) or $s_i < 0$ ($\beta_i < 0$), respectively. After substituting solution (19) into the linearized streamfunction-vorticity-energy equations, the following two ordinary differential equations are obtained:

$$i\alpha Re[(U_0 - s)(\psi_1'' - \alpha^2\psi_1) - U_0''\psi_1] = \\ \psi_1^{(IV)} - 2\alpha^2\psi_1'' + \alpha^4\psi_1 - Ha\left(\frac{a}{b}\right)^2(\psi_1'' - \alpha^2\psi_1) - \frac{Gr}{Re}\theta', \tag{20}$$

$$i\alpha RePr\left[(U_0 - s)\theta_1 - \theta_0'\psi_1\right] = \theta_1'' - \alpha^2\theta_1 - \psi_1', \tag{21}$$

which, along with the no-slip and thermal insulation boundary conditions,

$$y = \pm 1 : \psi_1 = \psi_1' = \theta_1' = 0 \tag{22}$$

constitute an eigenvalue problem for the complex parameter s. For a pure hydrodynamic isothermal flow Eqs. (20)–(22) transform to the classical OS problem for the plane Poiseuille flow. The main goals of the linear stability analysis are then to find conditions where $s_i = 0$ to determine the stability limit, and to find the wavelength giving the highest amplification rate. It is also useful to derive an equation for the kinetic energy of the pulsating motion, $K = 0.5\left\langle U_1^2 + V_1^2\right\rangle$ ("$\langle\rangle$" denotes averaging), and then to look at different terms on its right-hand side:

$$\frac{\partial K}{\partial t} + U_0\frac{\partial K}{\partial x} + V_0\frac{\partial K}{\partial y} = P_{K1} + P_{K2} + D + \varepsilon_v + \varepsilon_{Ha}. \tag{23}$$

The first term P_{K1} represents the shear production of kinetic energy, which is the product of the Reynolds stress and the mean flow strain rate. This shear production is identical to that in isothermal flows. The second term P_{K2}, whose main part is $\langle U'\theta'\rangle$, is another production term associated with temperature pulsations. The third term D is diffusion. The two last terms stand for dissipation losses: ε_v represents viscous dissipation in the bulk flow, while ε_{Ha} represents ohmic and viscous losses at the Hartmann walls, which are specific to Q2D MHD flows. In relation to the two production terms, in hydrodynamic buoyancy-driven flows, there have been identified two instability types (for references see Ref. 14). In the first type, which was found primarily for lower Prandtl-number fluids, the instability is initiated when the basic velocity profile is distorted sufficiently by buoyant forces to form an inflection point such that most of the kinetic energy for the instability comes from the shear production. This mode is termed as *thermal-shear instability*. The second type, which dominates in higher Prandtl-number fluids, obtains its energy primarily from temperature fluctuations. This type is called *thermal-buoyant instability*. The reason that lower Prandtl-number fluids do not exhibit thermal-buoyant instability is damping of temperature fluctuations due to high thermal conductivity of the fluid. In liquid metals, which are primarily coolants in fusion applications, $Pr \ll 1$. This suggests domination by thermal-shear instability in the blanket flows. All results computed in this paper are in fact limited to a particular value of the Prandtl number (0.01) typical to most liquid metals. For such a low Prandtl number both linear and nonlinear computations have confirmed that the dominating instability type is thermal-shear instability.

A pseudospectral MATLAB code, which eliminates spurious eigenvalues (Ref. 15), is used to solve the present OS problem. The code has been validated against available literature results, including linear stability of a plane Poiseuille flow (Ref. 16) as well as stability of the Hartmann (Ref. 17) and Shercliff layers (Ref. 18). A similar code was also used by authors of the present paper in Ref. 3. The neutral stability curves for two Hartmann numbers (50 and 100) and three Grashof numbers (10^7, 10^8, and 10^9) are shown in Fig. 5. Depending on Ha and Gr there can be one, two, or even three branches of the neutral curve. The flow is linearly unstable within the area bounded by the neutral curves and linearly stable outside. The figure also shows values of the amplification factor β_i inside each instability area. Similar to Ref. 3, two instability modes have been observed that are associated either with the inflection point in the basic velocity profile in the flow bulk (*bulk instability*, *BI*) or with the boundary layer at each side wall (*side-wall instability*, *SWI*). The bulk instability is of the Kelvin-Helmholtz type (also known as inflectional instability), whereas the side-wall instability is related to propagation of Tollmien–Schlichting waves. The SWI branches in Fig. 5 are always situated to the right of the BI branch. This means that SWI starts at higher

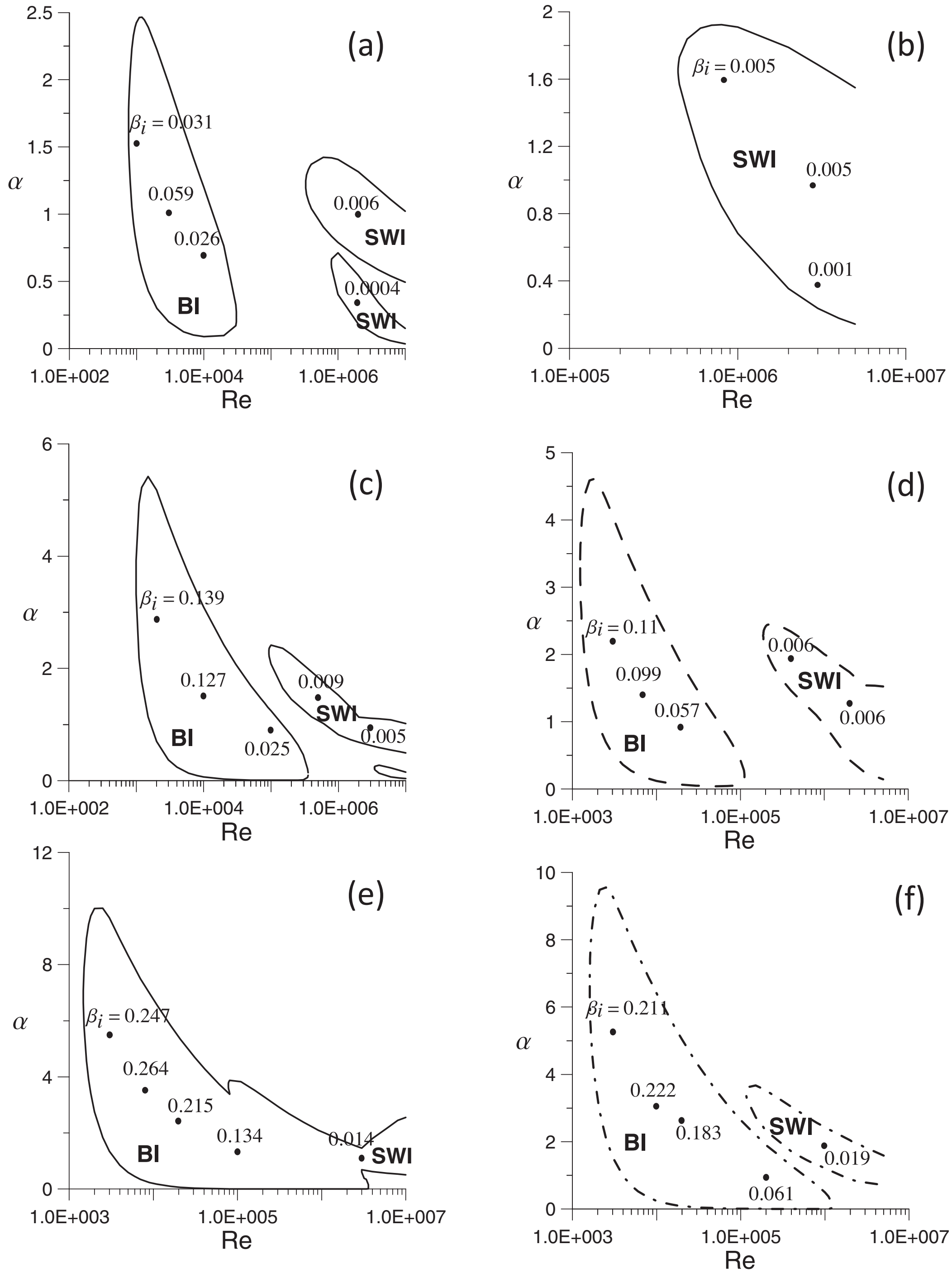

FIG. 5. Neutral stability curves with indication of bulk (BI) and side-wall (SWI) instabilities at: (a) $Ha = 50$, $Gr = 10^7$; (b) $Ha = 100$, $Gr = 10^7$; (c) $Ha = 50$, $Gr = 10^8$; (d) $Ha = 100$, $Gr = 10^8$; (e) $Ha = 50$, $Gr = 10^9$; and (f) $Ha = 100$, $Gr = 10^9$.

Reynolds numbers compared to BI when the basic velocity profile is only slightly deformed by buoyancy effects such that there are no inflection points, or if such points are nevertheless formed, the vorticity level at the inflection points is not high enough for inflectional instability to form.

The two branches in Fig. 5(a) located at $Re \sim 10^6$ stand for the SWI mode. The lower branch of these two exhibits longer wavelengths (smaller α) but a smaller amplification rate compared to

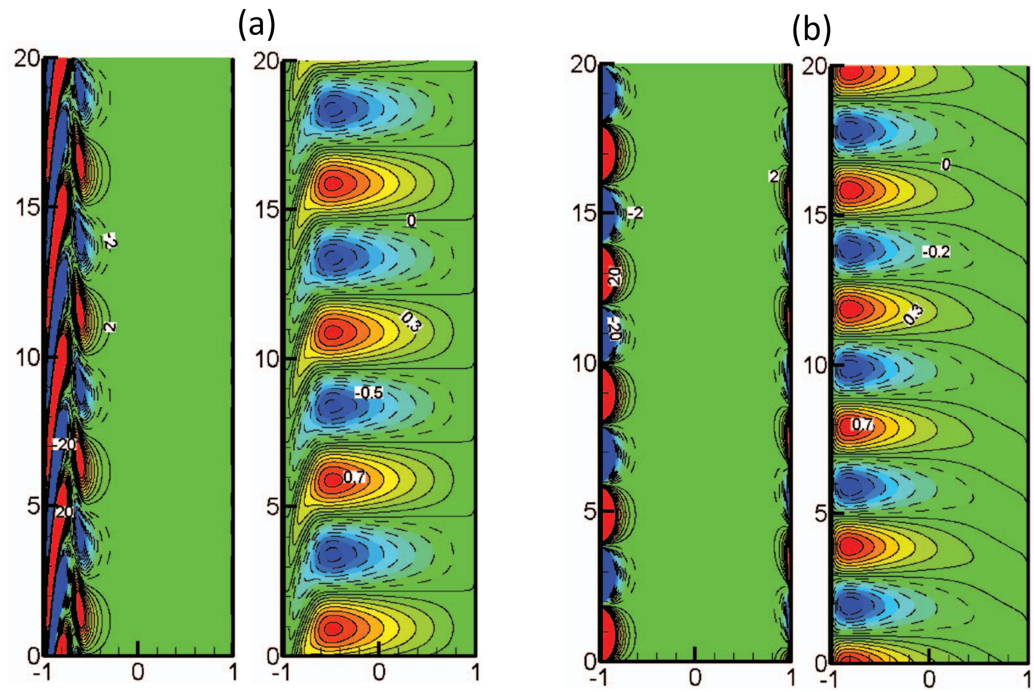

FIG. 6. Vorticity (left) and streamfunction (right) distributions in the reference mixed-convection flow based on the linear analysis for the most amplified perturbation mode: (a) bulk instability at $Ha = 100$, $Gr = 10^8$, $Re = 10^4$; (b) side-wall instability at $Ha = 100$, $Gr = 10^8$, $Re = 10^6$.

the other SWI branch. This branch fully disappears at higher Hartmann or Grashof numbers. The observed two SWI branches are consistent with similar observations in Ref. 18, where the case of purely Shercliff layers was studied using the same linear approach.

The differences between BI and SWI modes are well seen, for instance, in the vorticity distribution shown in Fig. 6. In the case of the side-wall instability, there is just one row of counter-rotating vortices, all localized at the wall within the boundary layer. This instability typically occurs at higher Reynolds numbers and has about one order of magnitude lower amplification factor compared to the bulk instability. In the case of the bulk instability, there are two rows, one to the right and one to the left of the inflection point. Usually, the inflection point is located on the bulk side of the velocity jet, close to the wall, such that the outer row of vortices is located in the near-wall region, where the velocity changes from zero at the wall to the maximum. Figure 6 also shows significant asymmetry in the vorticity distribution. Typically, instability happens at both the hot and cold walls but it is always more intensive at the hot wall in both SWI and BI cases. The significant differences between SWI and BI modes can also be observed in the streamfunction distributions also shown in Fig. 6.

As seen in Fig. 5, the BI and SWI can happen under the same conditions, for example, at the same Reynolds number. In such cases, the SWI mode always exhibits shorter wavelengths. This suggests that in real flows, these two instability modes can co-exist since original disturbances can be of any frequency. In some cases, however, the two neutral curve branches are fully separated suggesting only one instability mode as also demonstrated in Fig. 7, where the neutral curves are plotted in the 3D form.

The differences between BI and SWI are further illustrated in Fig. 8 in the form of dispersion curves. This figure clearly demonstrates either two instability modes happening at the same Reynolds number but at different wavelengths or just one mode.

The rate of growth of infinitesimal disturbances with time in the linear phase is best characterized with the parameter β_i. The effect of Gr, Re, and Ha numbers on this parameter is illustrated in Fig. 9. As the Hartmann number is increased, the amplification rate always drops. The Grashof number has the opposite effect: the higher the Gr, the higher is the amplification rate. The effect of the Reynolds

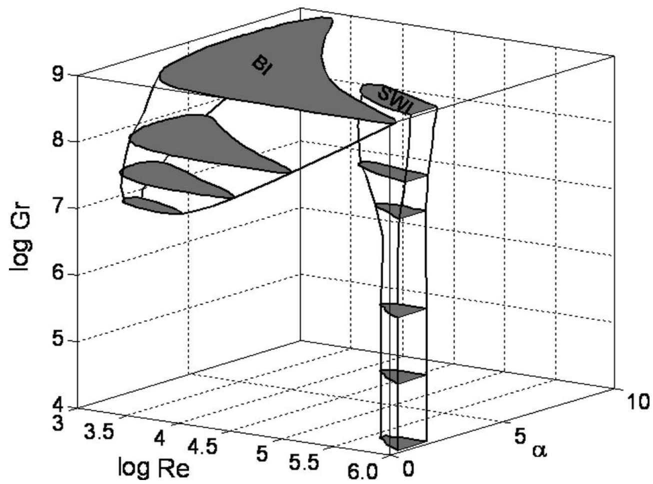

FIG. 7. Neutral surfaces (instability balloon) at $Ha = 100$ showing two types of instability regions (BI and SWI). The flow is linearly unstable inside each balloon and stable outside.

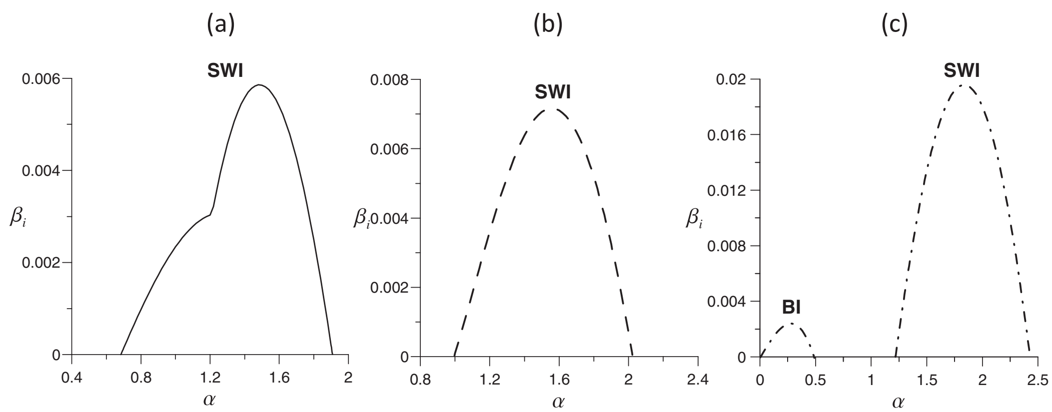

FIG. 8. Typical dispersion curves at $Ha = 100$, $Re = 10^6$: (a) $Gr = 10^7$, (b) $Gr = 10^8$, and (c) $Gr = 10^9$.

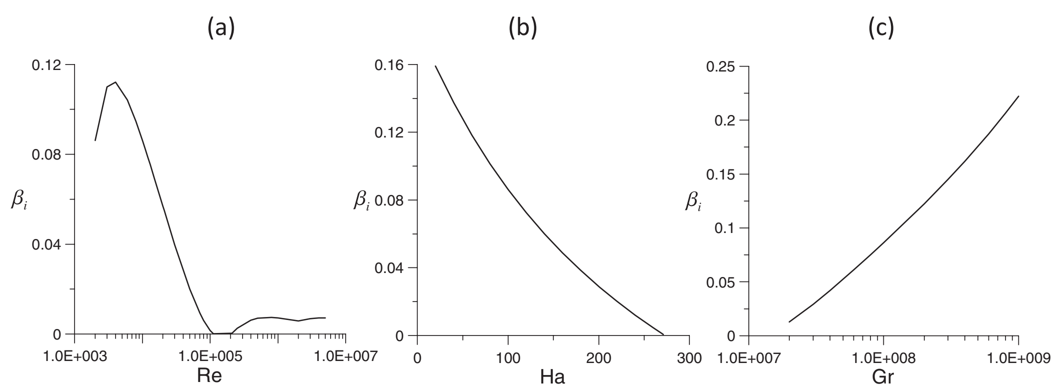

FIG. 9. Effect of the flow parameters on the amplification factor: (a) $Ha = 100$, $Gr = 10^8$; (b) $Re = 10\,000$, $Gr = 10^8$; and (c) $Ha = 100$, $Re = 10{,}000$.

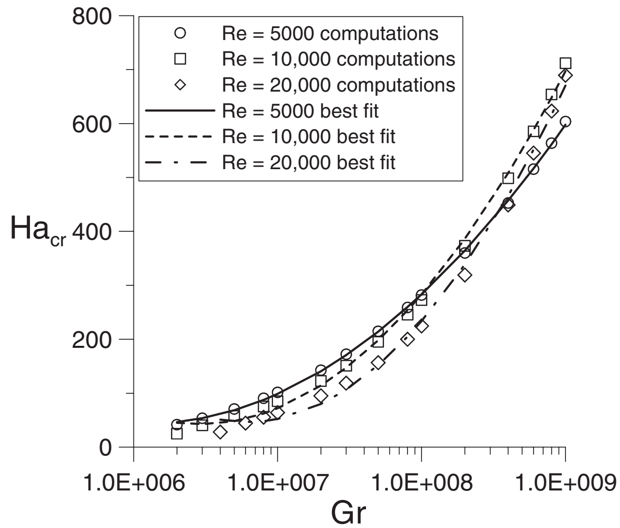

FIG. 10. Variation of the critical Hartmann number versus Grashof number at several *Re* numbers. Symbols stand for computations and lines for the best fit.

number is more complex. For example, for $Ha = 100$ and $Gr = 10^8$, β_i first increases with Re, then decreases to zero and after that starts increasing again. Such a complex behavior is related to changes in the instability type from BI to SWI. Finally, Fig. 10 shows the critical Hartmann number Ha_{cr} as a function of Grashof number at several Re numbers. For all Ha numbers greater than Ha_{cr}, the flow is linearly stable, whereas it is unstable if $Ha < Ha_{cr}$. The obtained data for Ha_{cr} can be approximated with the following formula:

$$Ha_{cr} = P_1(\log Gr)^2 + P_2 \log Gr + P_3, \tag{24}$$

where

$$P_1 = -5.98 \times 10^{-8} Re^2 + 2.284 \times 10^{-3} Re + 2.308,$$
$$P_2 = 1.8277 \times 10^{-6} Re^2 - 7.3037 \times 10^{-2} Re - 22.787,$$
$$P_3 = -1.37 \times 10^{-5} Re^2 + 0.57516 Re - 95.8.$$

Notice that applicability of this formula is guaranteed under specific conditions assumed in the present study, namely, for $5000 < Re < 20\,000$ and Gr from 10^6 to 10^9. It should be mentioned that the proposed correlation is just the best fit to the obtained numerical data and this particular form, using logarithms, is not supported by any physical arguments.

V. NONLINEAR COMPUTATIONS

Once the amplitude of perturbations becomes big enough, the nonlinear flow behavior often turns out to be very different from that predicted by the linear theory. To address nonlinear features we perform DNS-like computations by solving time-dependent Eqs. (16)–(18) over a long period of time and applying periodic boundary conditions at the flow inlet/outlet. A computer code, briefly described in Ref. 3, extends a standard time-marching $\psi - \omega$ approach to the reference case to take into account MHD and buoyancy effects. The governing equations are approximated with finite-volume formulas on a mesh, which is uniform in the axial direction and non-uniform in the cross-axial direction. The mesh clusters point near the wall within the side-wall boundary layers. At least ten points are placed within each boundary layer. The discretization is of a second-order accuracy in time and space. Advancing in time is performed using an Adams-Bashforth scheme. Central-difference formulas are used for the discretization of the diffusive terms in the ω-, ψ-, and θ-equations. For the convective terms, a conservative scheme proposed by Arakawa (Ref. 19) is used. This scheme, which conserves the basic quadratic quantities, such as the mean kinetic energy and

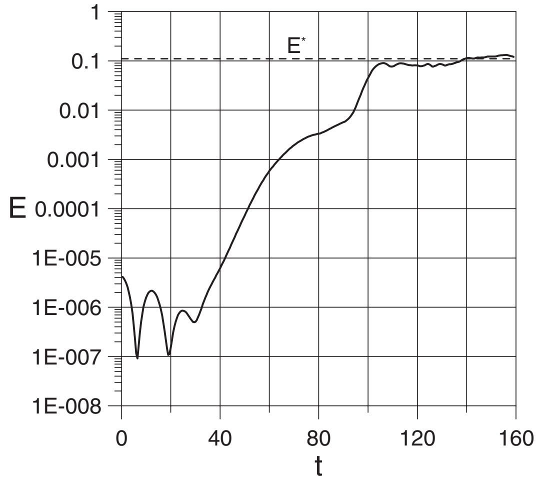

FIG. 11. Typical variation of the kinetic energy of the fluctuating flow versus time at $Ha = 50$, $Gr = 10^8$, and $Re = 5000$.

the mean enstrophy, allows for accurate computations of the nonlinear terms in 2D turbulent flows. Periodic boundary conditions are applied at the flow inlet and outlet, while no-slip and zero-heat-flux boundary conditions are used at the walls $y = \pm 1$. Using periodic boundary conditions when solving the elliptic equation for the streamfunction allows for implementation of a direct algorithm based on the fast Fourier transform (FFT), which is much faster and more accurate compared to most of the relaxation techniques.

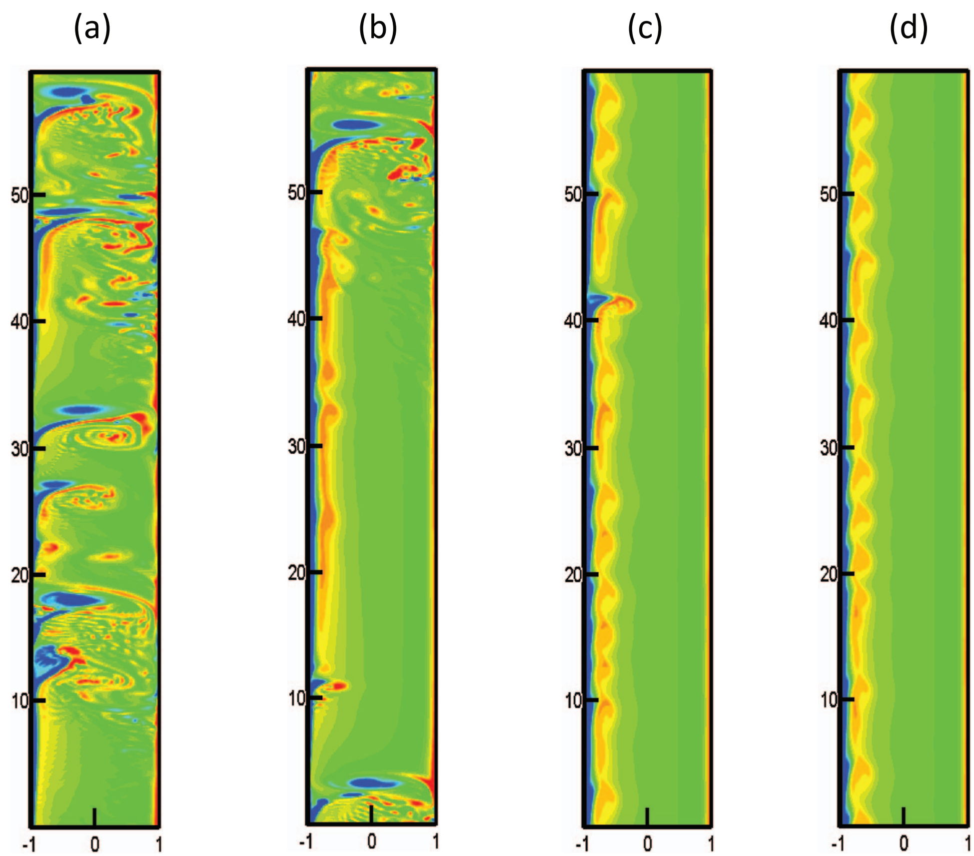

FIG. 12. Vorticity snapshots in the nonlinear saturation phase showing the effect of Ha number at $Re = 5000$ and $Gr = 10^8$: (a) $Ha = 50$, (b) $Ha = 60$, (c) $Ha = 100$, and (d) $Ha = 120$.

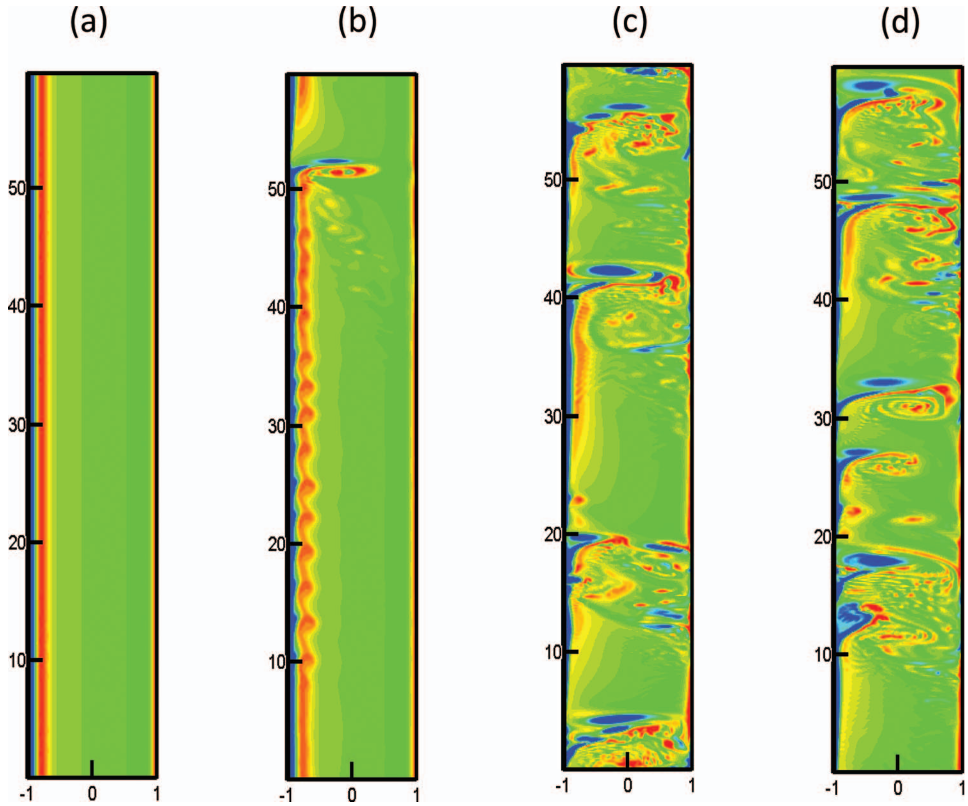

FIG. 13. Vorticity snapshots in the nonlinear saturation phase showing the effect of Re number at $Ha = 50$ and $Gr = 1 \times 10^8$: (a) $Re = 2000$, (b) $Re = 3000$, (c) $Re = 4000$, and (d) $Re = 5000$.

The nonlinear computations have been performed for $40 < Ha < 200$, $2000 < Re < 10\,000$, and $10^6 < Gr < 5 \times 10^8$ to address the effect of these parameters on the flow. For these parameters $D < 0$, suggesting basic velocity profiles with a distinctive high-velocity jet near the hot wall. These relatively low values of Re, Ha, and especially Gr compared to those in fusion applications are explained by computational limitations, on the one hand and, on the other hand, by limitations of the Q2D model itself as discussed in Sec. II. However, it seems to be appropriate to extrapolate observed tendencies in the flow to higher values relevant to blanket conditions, providing the major limitations of the Q2D theory are still met. Although the Q2D approach is very economical compared to full 3D computations, still there are limitations on Q2D computations for high Grashof numbers. In fact, the maximum Grashof number achieved in the Q2D computations is 5×10^8. This limitation turns out to be related to the well-known CFD problem (see, e.g., Ref. 20) of "mesh Reynolds/Peclet number" (in the context of the reference buoyancy-driven flows "mesh Grashof number"). On the other hand, limitations on Ha numbers are not critical such that high Hartmann number computations can be performed, providing the side-wall boundary layers are properly resolved. Limitations on the Reynolds number are mostly related to the Q2D model itself (not to the code), which requires the Hartmann layers to remain laminar.

In the computations, the flow domain is as long as 60 length units, which is sufficiently large to accommodate many wavelengths as computed with the linear stability analysis for the most amplified modes. Tests computations were also performed for a flow domain of 120 length units. No pronounced differences in flow patterns, characteristic wavelengths, and integral and statistically averaged flow parameters between these two computations were observed. As a result of sensitivity tests, a mesh of 512 (along the flow) by 201 points (across the flow) and the integration time step $\Delta t = 0.0005$ were chosen. In these tests, other meshes, such as 256 by 201, 256 by 401, 512 by 201, 512 by 101, and 1024 by 201 as well as two more time increments $\Delta t = 0.001$ and

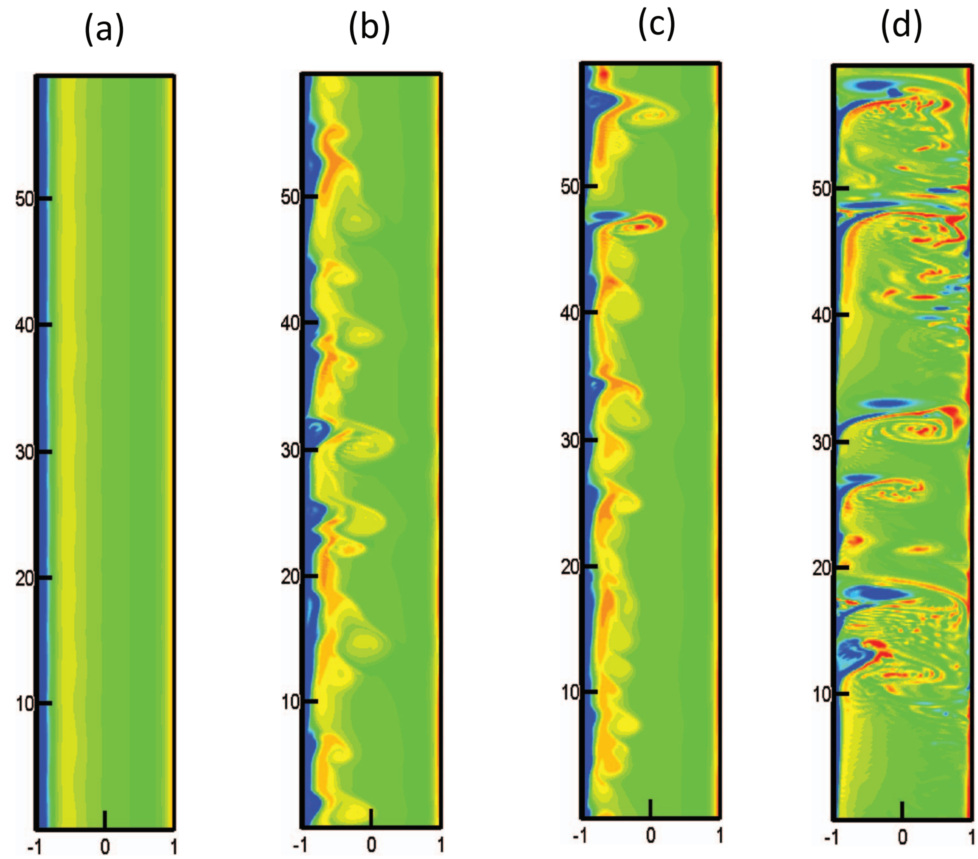

FIG. 14. Vorticity snapshots in the nonlinear saturation phase showing the effect of Gr number at $Ha = 50$ and $Re = 5000$: (a) $Gr = 10^7$, (b) $Gr = 5 \times 10^7$, (c) $Gr = 7 \times 10^7$, and (d) $Gr = 10^8$.

$\Delta t = 0.00025$ were used. At the initial moment the flow is disturbed by small perturbations, random in space, which are imposed on the basic flow streamfunction, without disturbing the vorticity field. For undisturbed flows, the Q2D solutions fully coincide with the 1D solution of Sec. III.

Typical changes of the mean kinetic energy defined as

$$E(t) = \frac{1}{2l} \int_0^l dx \int_{-1}^{1} 0.5 \left[(U - U_m)^2 + V_1^2 \right] dy \tag{25}$$

versus the computational time are shown in Fig. 11.

During a short initial phase ($t < 30$) the kinetic energy is small and fluctuating. The fluctuations in E seem to be related to the effect of the initial condition, where perturbation modes are randomly distributed. In the next phase ($30 < t < 60$), the flow demonstrates nearly linear behavior that corresponds to the exponential growth in time of the most amplified mode. This linear behavior is followed by a transitional phase ($60 < t < 100$), where nonlinear effects become more and more dominant, manifested, for example, by various vortex-vortex and vortex-wall interactions. Finally, as a result of intensive vortex formation and simultaneous energy dissipation, the flow reaches a nonlinear saturation phase ($t > 100$), where the averaged energy E remains at about the same level E^*, whereas the flow demonstrates pulsating near-periodic behavior in both time and space. This regime can be considered as a new dynamic equilibrium state in which the averaged flow no longer varies.

Examples of flows in the nonlinear saturation phase are given in Fig. 12, where the vorticity snapshots are shown at several Hartmann numbers.

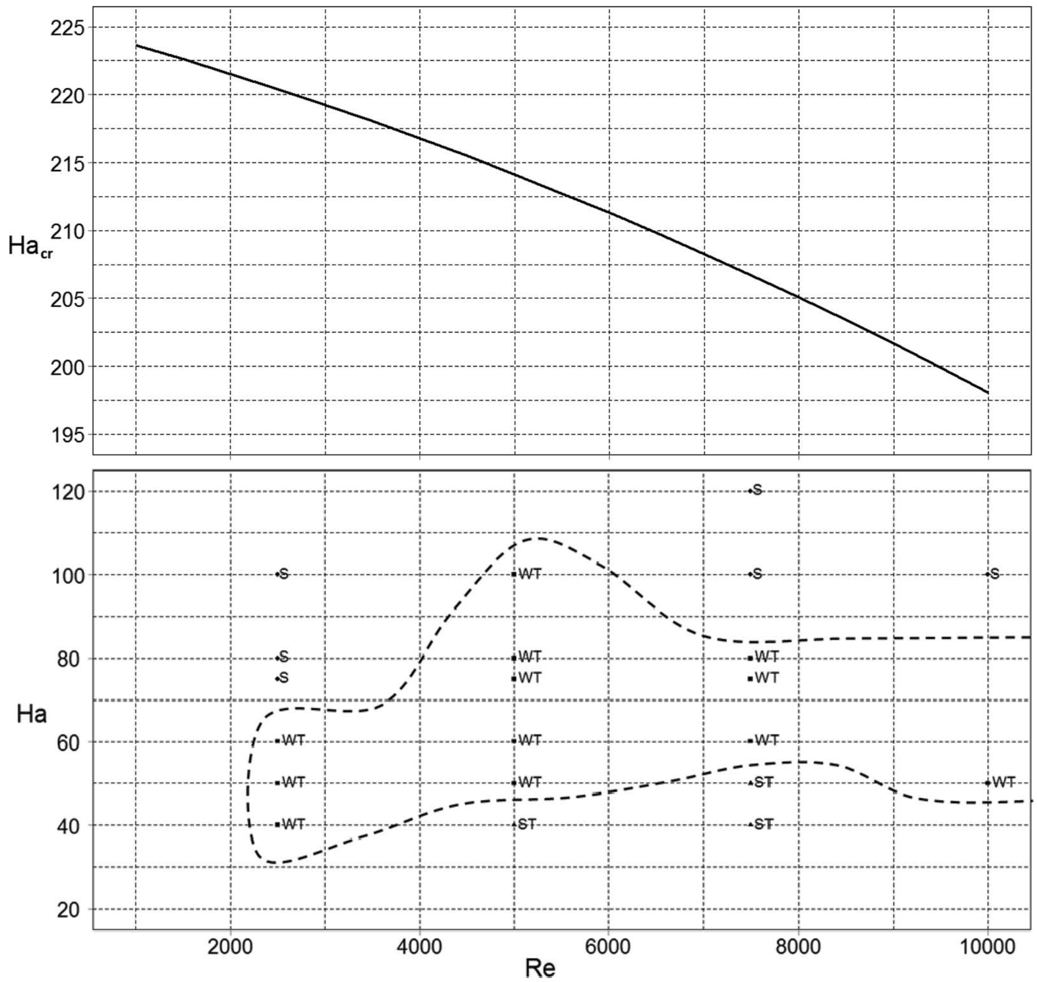

FIG. 15. (Bottom) Flow map showing laminar and two turbulent regimes in the *Ha*–*Re* plane for $Gr = 5 \times 10^7$. S—stable laminar flow, WT—weak turbulence, and ST—strong turbulence. (Top) Predictions of the critical Hartmann number with the linear theory.

These and other similar snapshots in Figs. 13 and 14 clearly demonstrate two different turbulence regimes, which we call "*strong turbulence*" (ST, e.g., Figs. 12(a) and 12(b)) and "*weak turbulence*" (WT, e.g., Fig. 12(c) and 12(d)). In the WT regime, the vortices are mostly formed from the original shear layer in the bulk flow near the hot wall. They remain localized in the same near-wall area where the basic velocity profile has an inflection point. Although the flow in the WT regime is not linear, the typical length scales associated with the bulk vortices can be predicted with the linear theory. Some nonlinear vortex-wall interactions are nevertheless clearly seen resulting in destabilization of the side-wall boundary layer, but neither separation of the boundary layer from the wall nor formation of isolated vortices can be seen.

In the ST regime, the most peculiar phenomenon is formation of turbulent streaks, which are clearly seen in Figs. 12(a), 13(c), 13(d), and 14(d). These processes are essentially nonlinear such that characteristic length scales, for example, the distance between two streaks, cannot be predicted with the linear theory. In this regime, the two characteristic features are intensive vortex-vortex and vortex-wall interactions. The vortex-wall interactions occur between the primary bulk vortices and the near-wall liquid. These interactions cause destabilization of the boundary layer and eventually its detachment from the wall at several locations along the flow path. This process involves a few characteristic stages. It is initiated first by a local concentration of the vorticity field within the side-wall boundary layer as a single bulk vortex or a group of vortices move along the wall. This

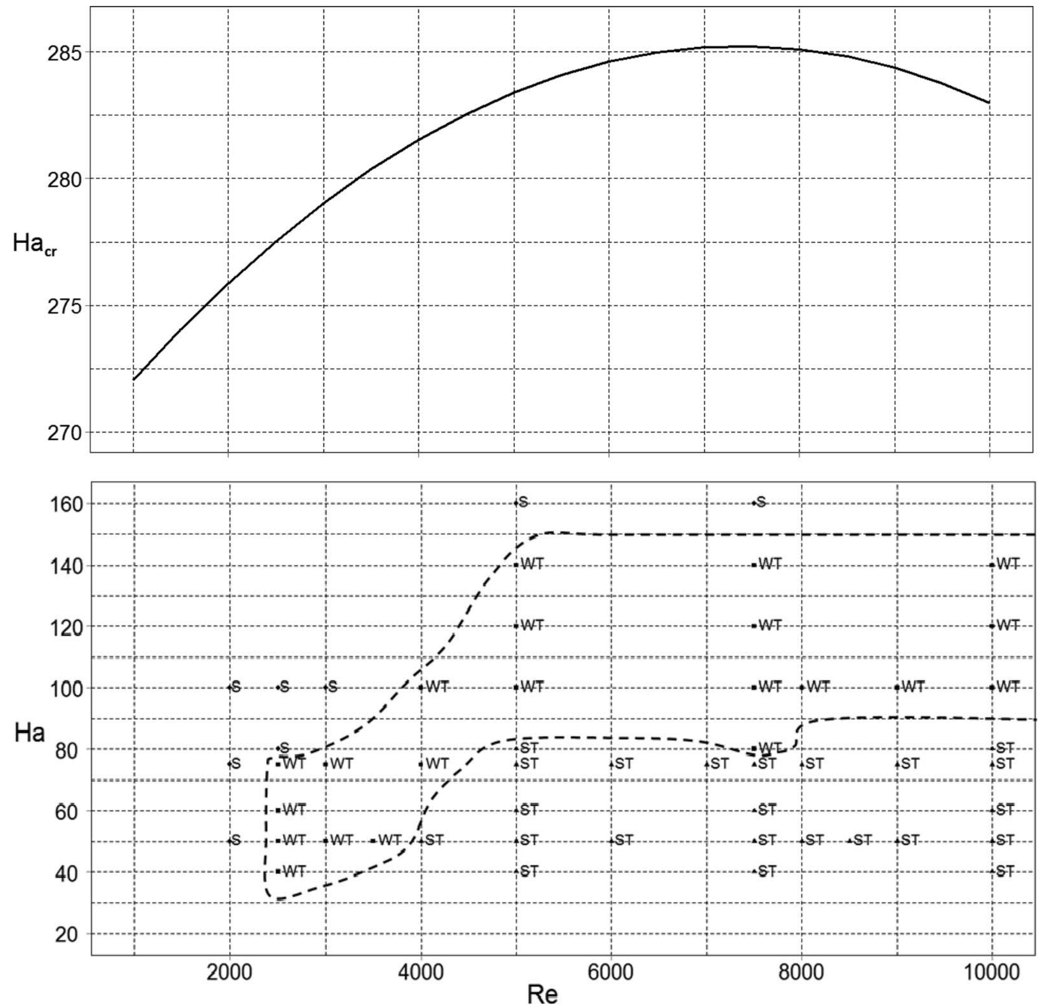

FIG. 16. (Bottom) Flow map showing laminar and two turbulence regimes in the *Ha*–*Re* plane for $Gr = 10^8$. (Top) Predictions of the critical Hartmann number with the linear theory. See also notations in Fig. 14 caption.

stimulates rapidly rising thin spires (streaks) of fluid that ultimately interact strongly with the external flow. These structures typically contain concentrated vorticity and often roll up into new, secondary, vortex structures. These newly developed vortices can travel far from their original location reaching sometimes the opposite wall and destabilizing its boundary layer.

The vortex-vortex interactions in the ST regime occur between various vortices, including primarily bulk vortices and secondary vortices, which are formed due to the destabilization of the side-wall boundary layer by the bulk vortices. These interactions are typical to Q2D turbulence as required by the inverse energy cascade and include pairing vortices of opposite signs and merging two or more vortices of the same sign into a bigger compound vortex structure, comparable in size with the duct width, as also seen in Figs. 12–14.

Changing the other two parameters, *Re* and *Gr* (Figs. 13 and 14), has not revealed any new peculiarities in the vorticity field in addition to those observed in Fig. 12. Depending on the 3 parameters either WT or ST regimes can be seen. However, increasing *Ha* always leads to the reduction of the kinetic energy, transition from strong to weak turbulence and finally to flow laminarization. Unlike the Hartmann number effect, increasing *Re* and *Gr* leads to more turbulent flows. Visualization of vorticity snapshots (e.g., shown in Figs. 12–14) along with the analysis of the mean kinetic energy E^* in the nonlinear saturation phase suggest that the turbulence can be considered as strong if $E^* > E_{cr} = 2 \times 10^{-2}$. This threshold value is not affected by the size of the flow domain, providing

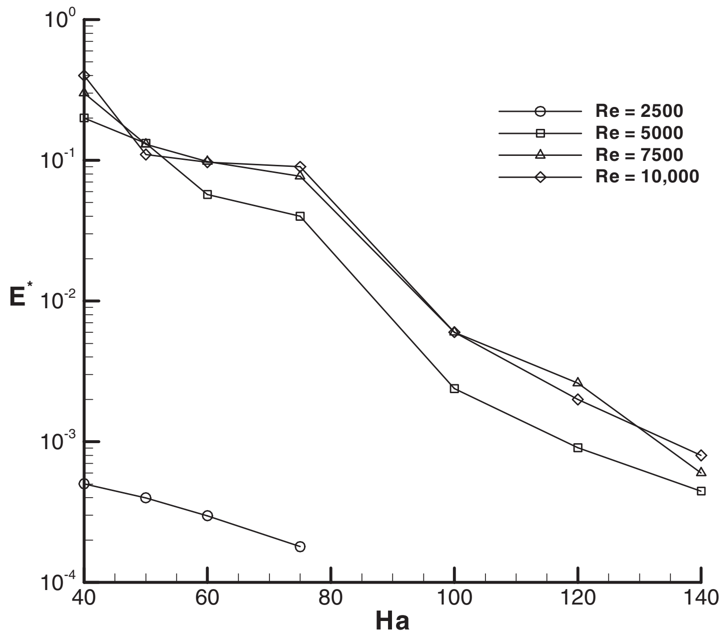

FIG. 17. Variation of the kinetic energy with Ha for different Re at $Gr = 10^8$.

the domain is long enough as in the computed cases of 60 length units. This criterion is further used in order to characterize the effect of these parameters on the turbulent flow regime. Two flow maps are shown in Figs. 15 and 16, where regions corresponding to ST and WT regimes are shown in the *Ha*–*Re* plane for two Grashof numbers. Also, at the top of these two figures the critical Hartmann number Ha_{cr} calculated with Eq. (24) is shown.

These figures clearly demonstrate that the linear theory significantly overpredicts the stability threshold. The tendency of the OS theory to overpredict critical parameters in the duct flows that characterize flow stability and poor agreement with experimental and numerical data is well known (see, e.g., Ref. 21), so that the present observation is fully consistent with previous conclusions.

Figures 17–19 illustrate changes in the kinetic energy E^* in the nonlinear saturation phase as a function of *Re*, *Gr*, and *Ha*. As the Hartmann number is increased, the kinetic energy drops monotonically to zero (Fig. 17). The increase in *Re* leads to the kinetic energy growing until the saturation level is achieved, which depends on the other two parameters (Fig. 18). The kinetic energy also grows as the *Gr* number is increased; however, any saturation in E^* with *Gr* for Grashof numbers up to 3×10^8 has not been observed (Fig. 19).

Figure 20 illustrates differences between the basic and turbulent flows where comparisons are shown for the velocity and temperature distributions. In the strong turbulence regime, such differences are much more pronounced compared to weak turbulence. In the weak turbulence regime, the changes in the velocity profile are mostly localized at the velocity peak associated with the near-wall jet, while in the strong turbulence regime the whole velocity profile is changed, not only near the hot wall but also in the bulk flow and at the cold wall. In both cases, turbulence results in a decrease of the maximum velocity and corresponding increase of the temperature near the hot wall.

Finally, Fig. 21 shows some heat transfer results. In this figure the space- (over the duct length) and time-averaged temperature difference between the temperature at the "hot" wall, θ_w, and that at the axis, θ_0, is plotted versus the Hartmann number. The figure also shows results from the analytical solution using 1D formulas derived in Sec. III. In the laminar flow case, the temperature difference increases with the Hartmann number due to reduction of the near-wall jet. The turbulent case demonstrates more complicated behavior, including both increase and decrease in the temperature differences as *Ha* number is increased. This behavior is related to two opposite

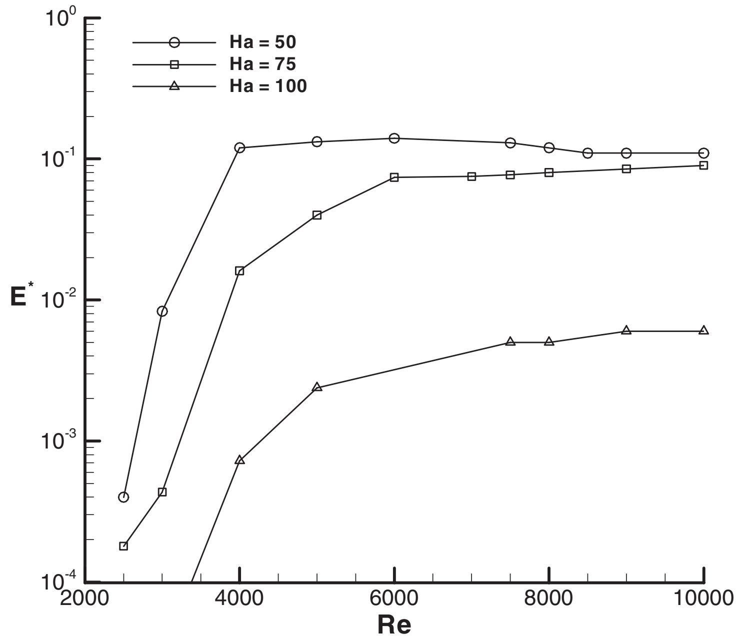

FIG. 18. Variation of the kinetic energy with Re for different Ha at $Gr = 10^8$.

heat transfer mechanisms. First, the temperature at the wall can drop as a result of the bulk vortex formation, their interactions with the side-wall boundary layer and turbulent streaks. Second, the temperature increases as the near-wall jet amplitude is reduced due to cross-axial turbulent transport of momentum. At high enough Ha the turbulent curve approaches the asymptotic laminar values.

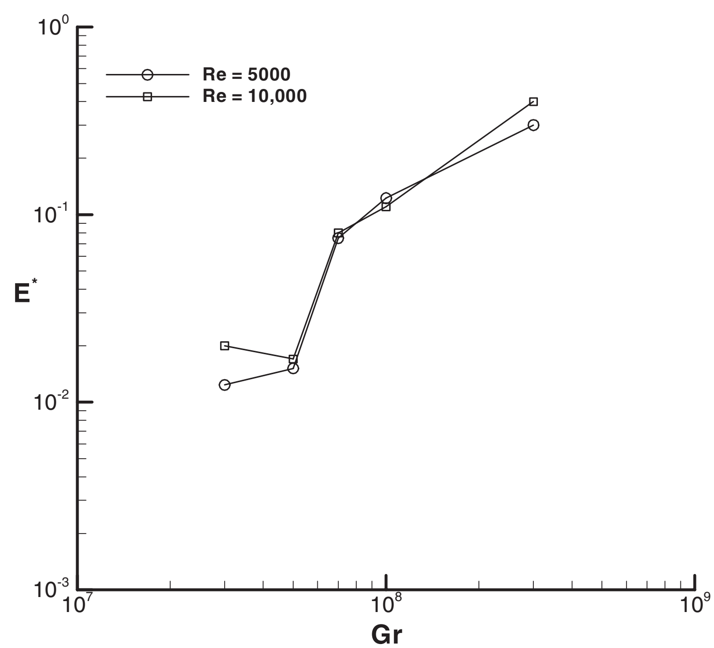

FIG. 19. Variation of the kinetic energy with Gr for different Re at $Ha = 50$.

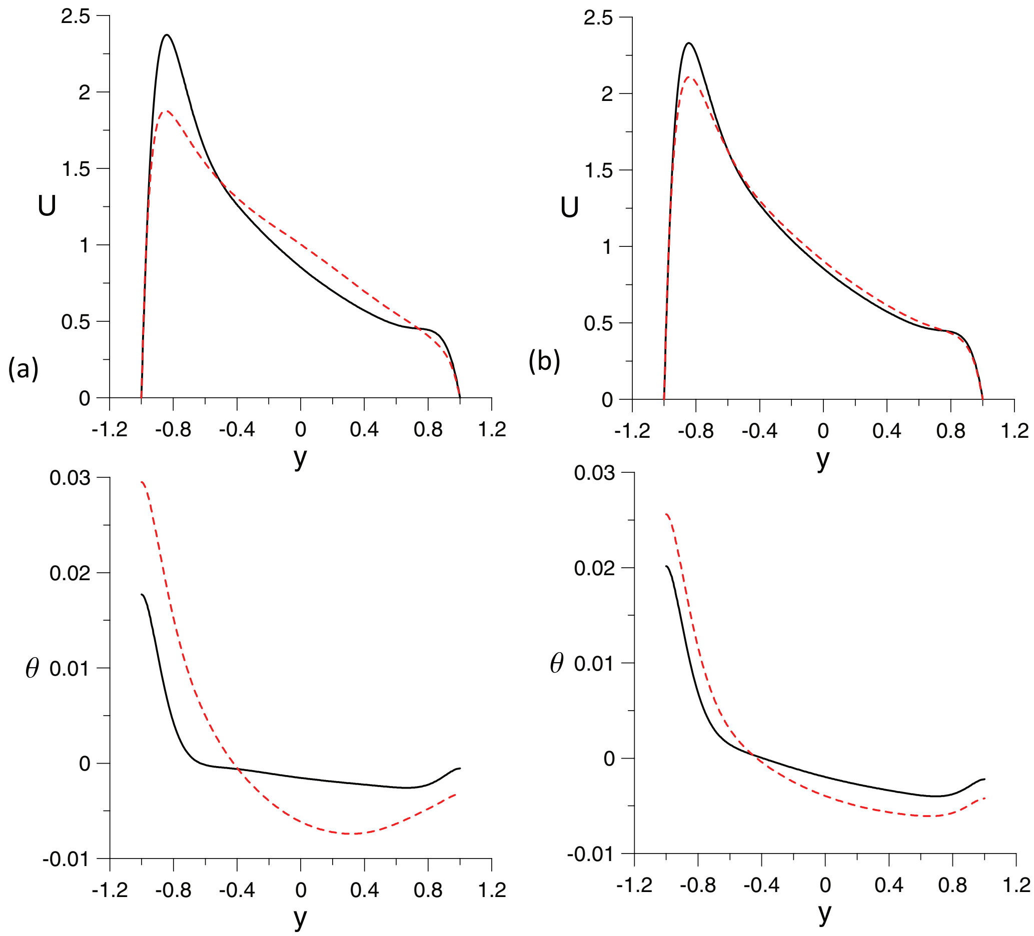

FIG. 20. Comparison of temperature and velocity profiles between basic (solid line) and turbulent (dotted line) flows: (a) strong turbulence at $Ha = 50$, $Gr = 10^8$, $Re = 5000$; (b) weak turbulence at $Ha = 100$, $Gr = 10^8$, $Re = 5000$.

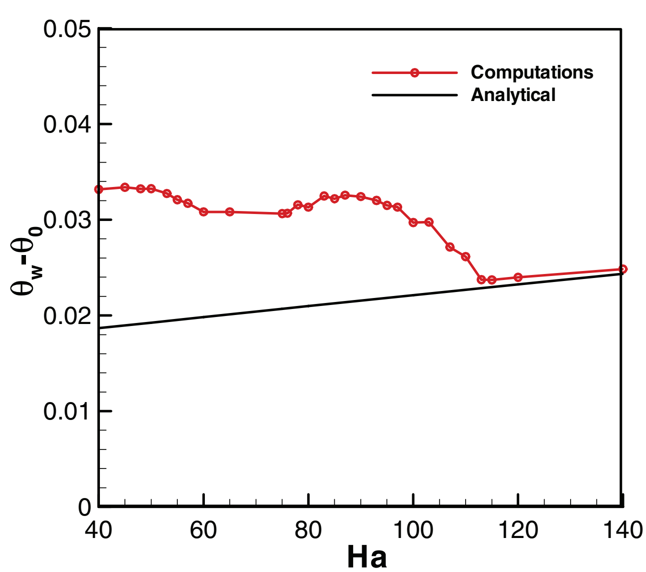

FIG. 21. Effect of the Hartmann number on the temperature difference between the "hot" wall and the axis at $Gr = 10^8$ and $Re = 5000$.

VI. CONCLUDING REMARKS

The linear theory predicts two instability modes: the bulk (inflectional) instability and the side-wall boundary layer instability. The instabilities mostly occur at the hot wall but in some cases also at the cold one. The instability mode is strongly dependent on the shape of the basic velocity profile, which can be characterized by parameters D and/or r introduced in Sec. III based on the analytical solution for the unperturbed flow. The side-wall boundary layer instability is more typical to high Reynolds number flows, where the basic velocity profile is just slightly distorted by the buoyancy forces. The observed instability is similar to the instability of the Shercliff layer in purely MHD flows. The bulk instability is more typical to MHD mixed-convection flows at relatively low Reynolds and high Grashof numbers such that the basic velocity profile demonstrates a high velocity jet near the hot wall and two or more inflection points. Typically, the bulk instability has a higher amplification rate than the side-wall instability (one order of magnitude higher) and smaller wavenumbers. In some cases, the linear theory suggests two instability modes can appear simultaneously. The bulk instability seems to be the most dominant linear instability type in the conditions of a fusion blanket. An important result from the linear stability analysis is Eq. (24), which allows for predicting a critical Hartmann number as a function of Gr and Re, above which the flow is linearly stable. Notice that applicability of this equation is not guaranteed far beyond the parameter range introduced in Sec. IV.

The nonlinear DNS-type computations allowed for the turbulent flow analysis. Upon reaching the nonlinear saturation phase in time, the flow demonstrates features typical to Q2D turbulence. Depending on Re, Ha, and Gr numbers, two characteristic turbulence regimes have been identified: (i) weak and (ii) strong turbulence. In the weak-turbulence regime, the vortices are mostly formed from the original shear layer in the bulk flow near the hot wall. They remain localized in the same near-wall area where the basic velocity profile has an inflection point. Some vortex-wall interactions are clearly seen but the boundary layer remains weakly disturbed. In the strong-turbulence regime, the two characteristic features are intensive vortex-vortex and vortex-wall interactions. The vortex-wall interactions cause the boundary layer destabilization and eventually its detachment from the wall at several locations along the flow path. The detached boundary layer and its interaction with the outer flow stimulate further formation of secondary vortices, which can travel across the whole flow reaching the opposite wall. The vortex-vortex interactions occur between various vortices, including primarily bulk vortices and secondary vortices in the form of pairing vortices of the opposite sign and merging two or more vortices of the same sign into a bigger compound vortex structure, comparable in size with the duct size. The transition from weak to strong turbulence can be characterized by the threshold kinetic energy [Eq. (25)] of 2×10^{-2}.

The observed two turbulence regimes seem to be similar to two instability types previously observed in other studies of MHD flows with the inflectional basic velocity profile, including Refs. 3 and 22–25. This suggests that the inflectional instability followed by the vortex-wall interactions are the two principal mechanisms in this type of MHD flow. However, the case of the mixed-convection flows demonstrates some differences from other studies, mostly due to a strong asymmetry in the velocity profile caused by the buoyancy forces and due to close proximity of the inflection point to the wall. This difference can be seen, for example, in the changes of the kinetic energy once one of the parameters associated with unstable behavior, either Reynolds or Grashof number, is increased. Even in a weak turbulence regime the perturbed flows seem to demonstrate nonlinear behavior. In previous studies (Refs. 3 and 22–25) the transition from one to another instability type occurred as a jump in the kinetic energy once the Reynolds number reached a critical value. This does not happen in the reference case, where the kinetic energy demonstrates sharp but continues changes.

ACKNOWLEDGMENTS

We acknowledge support from the U.S. Department of Energy (DOE) and TITAN program under DOE Grant No. 00072621.

[1] J. Sommeria and R. Moreau, "Why, how and when MHD turbulence becomes two-dimensional," J. Fluid Mech. **118**, 507 (1982).

[2] S. Smolentsev, R. Moreau, and M. Abdou, "Characterization of key magnetohydrodynamic phenomena in PbLi flows for the US DCLL blanket," Fusion Eng. Des. **83**, 771 (2008).
[3] S. Smolentsev, N. Vetcha, and R. Moreau, "Study of instabilities and transitions for a family of quasi-two-dimensional magnetohydrodynamic flows based on a parametrical model," Phys. Fluids **24**, 024101 (2012).
[4] L. Bühler, "Laminar buoyant magnetohydrodynamic flow in vertical rectangular ducts," Phys. Fluids **10**, 223 (1998).
[5] T. Tagawa, G. Authié, and R. Moreau, "Buoyant flow in long vertical enclosures in the presence of a strong horizontal magnetic field. Part 1. Fully-established flow," Eur. J. Mech. B Fluids **21**, 383 (2002).
[6] G. Authié, T. Tagawa, and R. Moreau, "Buoyant flow in long vertical enclosures in the presence of a strong horizontal magnetic field. Part 2. Finite enclosures," Eur. J. Mech. B: Fluids **22**, 201 (2003).
[7] N. Vetcha, S. Smolentsev, and M. Abdou, "Stability analysis for buoyancy-opposed flows in poloidal ducts of the DCLL blanket," Fusion Sci. Technol. **60**, 518 (2011).
[8] N. Vetcha, S. Smolentsev, and M. Abdou, "Theoretical study of mixed convection in poloidal flows of DCLL blanket," Fusion Sci. Technol. **56**, 851 (2009).
[9] Y. B. Kolesnikov and A. B. Tsinober, "Magnetohydrodynamic flow in the region of a jump in the conductivity at the wall," Magnetohydrodynamics **8**, 61 (1972).
[10] N. B. Morley, M. J. Ni, R. Munipalli, P. A. Huang, and M. A. Abdou, "MHD simulations of liquid metal flow through a toroidally oriented manifold," Fusion Eng. Des. **83**, 1335 (2008).
[11] R. G. Lingwood and T. Alboussière, "On the stability of the Hartmann layer," Phys. Fluids **11**, 2058 (1999).
[12] S. Smolentsev, N. Vetcha, and R. Moreau, "MHD mixed convection in a rectangular duct: 3D, 2D and 1D solutions," in *Proceedings of the 8th International PAMIR Conference on Fundamental and Applied MHD*, edited by A. Alemany, J. P. Chopart, and J. Freibergs (CNRS, France, 2011), p. 79.
[13] S. Wolfram, *Mathematica: A System for Doing Mathematics by Computer* (Addison-Wesley, Boston, 1991).
[14] Y.-C. Chen and J. N. Chung, "The linear stability of mixed convection in a vertical channel flow," J. Fluid Mech. **325**, 29 (1996).
[15] W. Huang and D. M. Sloan, "The pseudospectral method for solving differential eigenvalue problems," J. Comput. Phys. **111**, 399 (1994).
[16] S. A. Orszag, "Accurate solution of the Orr-Sommerfeld stability equation," J. Fluid Mech. **50**, 689 (1971).
[17] R. C. Lock, "The stability of the flow of an electrically conducting fluid between parallel planes under a transverse magnetic field," Proc. R. Soc. London, Ser. A **233**, 105 (1955).
[18] A. Pothérat, "Quasi-two-dimensional perturbations in duct flows under transverse magnetic field," Phys. Fluids **19**, 074104 (2007).
[19] A. Arakawa, "Computational design for long-term numerical integration of the equations of fluid motion: Two-dimensional incompressible flow. Part I," J. Comput. Phys. **1**, 119 (1966).
[20] J. C. Tannehill, D. A. Anderson, and P. H. Pletcher, *Computational Fluid Mechanics and Heat Transfer* (Taylor & Francis, Washington, DC, 1997).
[21] L. N. Trefethen, A. E. Trefethen, S. C. Reddy, and T. A. Driscoll, "Hydrodynamic stability without eigenvalues," Science **261**, 578 (1993).
[22] C. B. Reed and B. F. Picologlou, "Sidewall flow instabilities in liquid metal MHD flows under blanket relevant conditions," Fusion Tech. **15**, 705 (1989).
[23] U. Burr, L. Barleon, U. Müller, and A. Tsinober, "Turbulent transport of momentum and heat in magnetohydrodynamic rectangular duct flow with strong sidewall jets," J. Fluid Mech. **406**, 247 (2000).
[24] L. Bühler and S. Horanyi, "Measurements of time-dependent liquid-metal magnetohydrodynamic flows in a flat rectangular duct," Fusion Eng. Des. **84**, 518 (2009).
[25] M. Kinet, B. Knaepen, and S. Molokov, "Instabilities and transition in magnetohydrodynamic flows in ducts with electrically conducting walls," Phys. Rev. Lett. **103**, 154501 (2009).